

A program for modeling the RF wave propagation of ICRF antennas utilizing the finite element method

Lei-Yu Zhang(张雷宇), Yi-Xuan Li(李屹轩), Ming-Yue Han(韩明月), and Quan-Zhi Zhang(张权治)

Citation: Chin. Phys. B, 2025, 34 (**4**): 045201. DOI: 10.1088/1674-1056/adaccc
Journal homepage: http://cpb.iphy.ac.cn; http://iopscience.iop.org/cpb

What follows is a list of articles you may be interested in

Three-dimensional simulations of RF wave propagation and power coupling in cold magnetized plasma near an ICRF antenna

Lei-Yu Zhang(张雷宇), Yi-Xuan Li(李屹轩), and Quan-Zhi Zhang(张权治)
Chin. Phys. B, 2025, 34 (**2**): 025204. DOI: 10.1088/1674-1056/ad9a9c

Characteristics of the electromagnetic wave propagation in magnetized plasma sheath and practical method for blackout mitigation

Xiang Wu(吴翔), Jiahui Zhang(张珈珲), Guoxiang Dong(董果香), and Lei Shi(石磊)
Chin. Phys. B, 2024, 33 (**5**): 055201. DOI: 10.1088/1674-1056/ad24d4

Damage characteristics of laser plasma shock wave on rear surface of fused silica glass

Xiong Shen(沈雄), Guo-Ying Feng(冯国英), Sheng Jing(景晟), Jing-Hua Han(韩敬华), Ya-Guo Li(李亚国), Kai Liu(刘锴)
Chin. Phys. B, 2019, 28 (**8**): 085202. DOI: 10.1088/1674-1056/28/8/085202

Surface plasmon-enhanced dual-band infrared absorber for VO_x-based microbolometer application

Qi Li(李琦), Bing-qiang Yu(于兵强), Zhao-feng Li(李兆峰), Xiao-feng Wang(王晓峰), Zi-chen Zhang(张紫辰), Ling-feng Pan(潘岭峰)
Chin. Phys. B, 2017, 26 (**8**): 085202. DOI: 10.1088/1674-1056/26/8/085202

Microwave absorption properties of Ag naowires/carbon black composites

Hai-Long Huang(黄海龙), Hui Xia(夏辉), Zhi-Bo Guo(郭智博), Yu Chen(陈羽), Hong-Jian Li(李宏建)
Chin. Phys. B, 2017, 26 (**2**): 025207. DOI: 10.1088/1674-1056/26/2/025207

COMPUTATIONAL PROGRAMS FOR PHYSICS

A program for modeling the RF wave propagation of ICRF antennas utilizing the finite element method

Lei-Yu Zhang(张雷宇), Yi-Xuan Li(李屹轩), Ming-Yue Han(韩明月), and Quan-Zhi Zhang(张权治)[†]

School of Physics, Dalian University of Technology, Dalian 116024, *China*

(Received 1 November 2024; revised manuscript received 15 January 2025; accepted manuscript online 22 January 2025)

Controlled nuclear fusion represents a significant solution for future clean energy, with ion cyclotron range of frequency (ICRF) heating emerging as one of the most promising technologies for heating the fusion plasma. This study primarily presents a self-developed 2D ion cyclotron resonance antenna electromagnetic field solver (ICRAEMS) code implemented on the MATLAB platform, which solves the electric field wave equation by using the finite element method, establishing perfectly matched layer (PML) boundary conditions, and post-processing the electromagnetic field data. This code can be utilized to facilitate the design and optimization processes of antennas for ICRF heating technology. Furthermore, this study examines the electric field distribution and power spectrum associated with various antenna phases to investigate how different antenna configurations affect the electromagnetic field propagation and coupling characteristics.

Keywords: ion cyclotron range of frequency (ICRF) antennas, finite element method, perfect matching layer

PACS: 52.25.Xz, 52.65.–y, 28.52.Av, 42.25.Bs

DOI: 10.1088/1674-1056/adaccc **CSTR:** 32038.14.CPB.adaccc

1. Introduction

Controlled nuclear fusion offers a promising solution for generating clean energy, with the tokamak as one of the most viable devices for realizing this technology. Ion cyclotron range of frequency (ICRF) heating is essential in existing fusion experiments[1–3] as one of the main technologies for heating plasma. Additionally, ICRF can assist in driving the plasma current,[4–9] supporting tokamaks in achieving steady-state operation. The ICRF antenna is a critical component of the RF heating system,[10] delivering significant power to the plasma. Optimizing its design and coupling with the plasma is essential to improve performance.[11] Enhancing the coupling efficiency of the ICRF antenna is a focus of researches.[12–14] Owing to the challenges associated with an actual antenna in the presence of plasma, it is essential to utilize numerical simulations to investigate the propagation of RF waves and the coupling processes within the cold plasma.

At present, a wide array of codes and software exists for simulating the propagation of electromagnetic waves generated by ICRF antennas and their coupling processes with cold plasma. Numerous researchers have utilized these codes and software to achieve noteworthy results. For instance, the Princeton Plasma Physics Laboratory developed the RANT3D code system to examine how antenna structures affect the power spectrum of antenna emissions within the ion cyclotron frequency range.[15] Qin *et al.*[11] employed the HFSS code to simulate a newly designed ICRF antenna, examining the impact of the number of antenna strips on the power spectrum and analyzing how antenna phase affects both the parallel RF electric field and sheath potential. Milanesio *et al.*[16–19] used the TOPICA code to simulate the ITER ICRF antenna with complex antenna geometries. Their work provided a detailed assessment of antenna performance across various frequencies and load conditions relevant to ITER. Pécoul *et al.*[11] modeled the antenna using finite current elements and performed self-consistent calculations of parameters such as the currents on the antenna band and the Faraday screen blades using the ICANT code. Their analyses yielded key metrics, including the antenna radiation power and frequency response. Usoltceva *et al.*[20,21] introduced a RAPLICASOL model that, for the first time, integrated a complete real density profile (excluding a vacuum layer) into the three-dimensional model of the ICRF antenna. This innovation facilitated the simultaneous propagation and absorption of both fast waves (FW) and slow waves (SW). Tierens *et al.*[22,23] validated the finite element code RAPLICASOL through comparison with the TOPICA code, demonstrating strong consistency in parameters such as reflection coefficient, coupling resistance, optimal matching settings, and RF electric field. Additionally, numerous researchers have applied commercial software to develop new models and conduct mutual verification of the results obtained from existing codes. Jacquot *et al.*[24,25] leveraged commercial software COMSOL to address compatibility issues related to simultaneously adapting to FW and SW propagations by utilizing a non-uniform density distribution. Yang *et al.*[26] adopted CST software to assess and compare the performance

[†]Corresponding author. E-mail: qzzhang@dlut.edu.cn

© 2025 Chinese Physical Society and IOP Publishing Ltd. All rights, including for text and data mining, AI training, and similar technologies, are reserved.

of two antenna designs: the folded antenna and the double loop one. However, the aforementioned code and software either lack adequate mesh refinement, resulting in convergence difficulties and time-consuming calculations, or fail to accurately simulate really magnetized plasma environments.

This study presents an efficient 2D ICRF antenna simulation code of "ICRAEMS" based on the MATLAB platform, allowing for fast calculations. The finite element method is utilized to solve the equations governing electric field waves with fine meshes, which can well resolve complex antenna geometry. Furthermore, a dielectric tensor based on the cold plasma approximation is used to account for the anisotropic characteristics of the magnetized plasma. Perfectly matched layer (PML) techniques are employed to address boundary issues related to electromagnetic field absorption, facilitating the simulation of electromagnetic field data radiated by the ICRF antenna in a limited geometry.

2. Simulation model

A self-developed 2D ICRF antenna simulation code named ICRAEMS has been utilized for the ICRF simulations. The model's algorithmic flow for solving the electric field wave equations in the frequency domain using the 2D (two-dimensional) finite element method near the ICRF antenna is illustrated in Fig. 1.

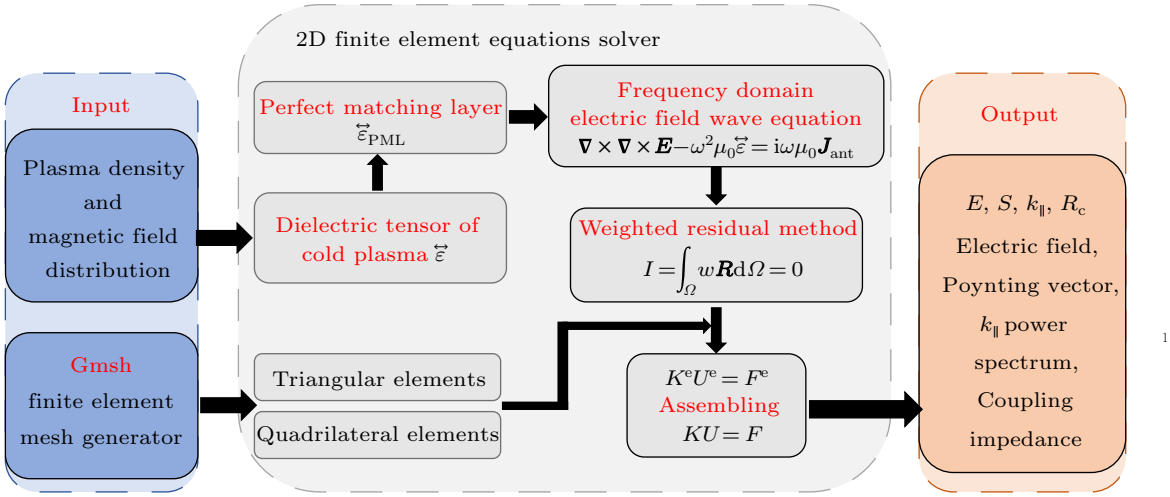


Fig. 1. Schematic flow diagram of the finite element algorithm for ICRF antennas.

The input module includes plasma and antenna parameters (geometric structure and mesh division files), while the output module primarily consists of the electric field, Poynting vector, $k_\parallel$ power spectrum, and coupling impedance. The main solution module of the code includes the calculation of the cold plasma dielectric tensor, PML setup, assembly of element matrices, finite element equation solving, and post-processing. A benchmark utilizing COMSOL software has been conducted based on the simulation of 2D ICRF under the same configuration. The results were nearly identical, with the ICRAEMS code demonstrating computation speeds that are slightly faster than COMSOL on our computer (Intel® Core™ i7-14700K, 128 GB RAM), thereby underscoring its reliability and efficiency. Additionally, the ICRAEMS code uses less memory due to its specific design for simulating ICRF. It can function as an independent module or be modified to accommodate alternative antenna configurations. Consequently, the ICRAEMS code may provide an advantage in scenarios where lower-specification computers are utilized, especially when compared to larger software or simulation platforms that typically require high-performance servers for optimal results.

The simulation area coordinates are defined within a 2D Cartesian coordinate system, where the x and y axes correspond to the toroidal and radial directions of the ICRF antenna, respectively. The dimensions of the simulation area are 2 m × 1 m. Geometric modeling and mesh division are performed using the open-source software Gmsh. Figure 2 presents a schematic representation of the model's geometry and mesh division.

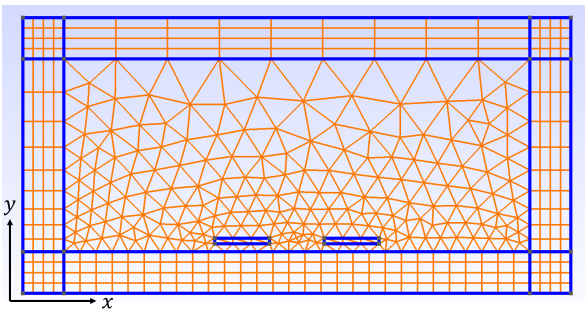


Fig. 2. Schematic diagram of the mesh for the simulation area, created by using the open-source software Gmsh. Note that a reduced number of elements is presented for clarity; a denser mesh comprising 34036 triangular element and 5024 quadrilateral element is actually utilized in the simulations.

Given the open nature of the simulation area, PML

boundary conditions are implemented around the perimeter to absorb electromagnetic waves that reach the boundaries, thereby implementing a single-pass model. Triangular meshes are employed for the antenna and electromagnetic field propagation regions, as this type of mesh effectively adapts to the complex geometries of antennas and allows for local mesh refinement. Inside the PML layer, regular quadrilateral meshes are utilized to optimize the performance of the PML, ensuring complete absorption of electromagnetic waves. In this study, the PML thickness is set to 0.15 m, with 8 layers of PML. The antenna structure features a toroidal double-current strap, with each strap measuring 0.2 m in width and 0.02 m in thickness. The spacing between the two antennas is 0.14 m, and their lower surface is positioned 0.18 m above the base in the y-direction. In a tokamak, the gradients of plasma density and magnetic field strength in the radial direction are significantly greater than those in the other two directions. Therefore, we assume a uniform distribution of plasma density and magnetic field strength along toroidal direction, while the spatial distribution in the y-direction is based on experimental measurements conducted on the EAST.[27] Furthermore, we assume that the magnetic field is strictly parallel to the x-direction, such that $B_x = B_0$.

2.1. Derivation of the dielectric tensor for cold plasma

In this model, plasma is treated as a medium, its equation for electric field wave in the time domain is solved as follows:

$$\nabla\times\nabla\times\boldsymbol{E} = -\mu_0\varepsilon_0\frac{\partial^2\boldsymbol{E}}{\partial t^2} - \mu_0\frac{\partial\boldsymbol{J}}{\partial t}. \tag{1}$$

Here, $\boldsymbol{E}$ denotes the electric field vector, μ_0 and ε_0 represent the permeability and permittivity of free space, respectively. And $\boldsymbol{J}$ signifies the current density vector. The current density can be further subdivided into plasma current ($\boldsymbol{J}_\mathrm{p}$) and antenna current ($\boldsymbol{J}_\mathrm{ant}$). Its electric field wave in the frequency domain is given by

$$\begin{aligned}\nabla\times\nabla\times\boldsymbol{E} &= \omega^2\mu_0\varepsilon_0\boldsymbol{E} + \mathrm{i}\omega\mu_0\boldsymbol{J}\\ &= \omega^2\mu_0\varepsilon_0\boldsymbol{E} + \mathrm{i}\omega\mu_0\left(\boldsymbol{J}_\mathrm{p}+\boldsymbol{J}_\mathrm{ant}\right),\end{aligned} \tag{2}$$

where $\omega = 2\pi f$, represents the radio frequency, and all the work has been performed at $f = 35$ MHz. According to the motion equations of electrons and ions in electric and magnetic fields, the plasma current density can be expressed as follows:

$$\frac{\partial\boldsymbol{J}_\mathrm{e}}{\partial t} = \frac{e^2 n}{m_\mathrm{e}}\boldsymbol{E} - \frac{e}{m_\mathrm{e}}\boldsymbol{J}_\mathrm{e}\times\boldsymbol{B} - \nu_\mathrm{ei}\boldsymbol{J}_\mathrm{e}, \tag{3}$$

$$\frac{\partial\boldsymbol{J}_\mathrm{i}}{\partial t} = \frac{e^2 n}{m_\mathrm{i}}\boldsymbol{E} + \frac{e}{m_\mathrm{i}}\boldsymbol{J}_\mathrm{i}\times\boldsymbol{B} - \nu_\mathrm{ie}\boldsymbol{J}_\mathrm{i}. \tag{4}$$

Here, $\boldsymbol{J}_\mathrm{e}$ and $\boldsymbol{J}_\mathrm{i}$ represent the electron and ion current densities, respectively. e denotes the charge of the electron, n refers to the plasma density, and m_e and m_i are the masses of the electron and ion, respectively. Additionally, $\boldsymbol{B}$ indicates the magnetic induction vector, while ν_ei and ν_ie represent the collision frequencies of electrons and ions, respectively. Under the cold plasma approximation, where the collision terms between electrons and ions are ignored (i.e., $\nu_\mathrm{ei} = \nu_\mathrm{ie} = 0$), the plasma current density can be formulated in terms of the electric field. This leads to the following relationship for the ion current density:

$$\frac{\partial\boldsymbol{J}_\mathrm{i}}{\partial t} = -\mathrm{i}\omega\boldsymbol{J}_\mathrm{i} = \frac{e^2 n}{m_\mathrm{i}}\boldsymbol{E} + \frac{e}{m_\mathrm{i}}\boldsymbol{J}_\mathrm{i}\times\boldsymbol{B}, \tag{5}$$

$$\Rightarrow -\mathrm{i}\omega\boldsymbol{J}_\mathrm{i} - \frac{e}{m_\mathrm{i}}\boldsymbol{J}_\mathrm{i}\times\boldsymbol{B} = \frac{e^2 n}{m_\mathrm{i}}\boldsymbol{E}. \tag{6}$$

Similarly, the relationship between the electron current density and the electric field can be derived. By expressing the current density as a function of the electric field and substituting this expression into the electric field wave equation, we obtain a modified wave equation that incorporates the dielectric tensor

$$\nabla\times\nabla\times\boldsymbol{E} - \omega^2\mu_0\overleftrightarrow{\varepsilon}\boldsymbol{E} = \mathrm{i}\omega\mu_0\boldsymbol{J}_\mathrm{ant}, \tag{7}$$

where the dielectric tensor[28]

$$\overleftrightarrow{\varepsilon} = \overleftrightarrow{\boldsymbol{I}} - \sum\nolimits_\alpha \begin{pmatrix} \frac{\omega_\alpha^2}{\omega^2} & 0 & 0 \\ 0 & \frac{\omega_\alpha^2}{\omega^2-\Omega_\alpha^2} & \left(\frac{\Omega_\alpha}{\mathrm{i}\omega}\right)\frac{\omega_\alpha^2}{\omega^2-\Omega_\alpha^2} \\ 0 & -\left(\frac{\Omega_\alpha}{\mathrm{i}\omega}\right)\frac{\omega_\alpha^2}{\omega^2-\Omega_\alpha^2} & \frac{\omega_\alpha^2}{\omega^2-\Omega_\alpha^2} \end{pmatrix}. \tag{8}$$

The dielectric tensor using the cold plasma approximation allows for the consideration of the anisotropic properties of the plasma. Given that the antenna plasma temperature is relatively low, cold plasma approximation is used to describe the dielectric tensor of the magnetized plasma.

2.2. PML configuration

In the solution region, effectively absorbing the energy of traveling waves at finite boundaries poses a challenge in the numerical simulation of wave propagation in infinite media. PML is a technique used to manage electromagnetic field boundaries. In this approach, wave propagation within the matching layer is attenuated, resulting in a reflection coefficient of zero for incoming waves at any angle and frequency.[29]

In the open space problem of ICRF modeling, the essence of the PML theory is to coordinate the PML used for stretching, allowing electromagnetic waves to attenuate at the edges of the computational domain. The stretched complex space is treated as infinite, which enhances wave attenuation in the finite space. Within the PML boundary, the coordinate transformation is achieved using the complex stretching function $s(x)$,[12]

$$\frac{\partial}{\partial\tilde{x}} = \frac{1}{s(x)}\frac{\partial}{\partial x}, \tag{9}$$

$$s_x(x) = \beta_x(x) + \frac{d_x(x)}{\alpha_x(x) + \mathrm{i}\omega}. \tag{10}$$

Here, $\tilde{x}$ represents the coordinates after the complex stretching transformation, d denotes the attenuation coefficient, β is the contraction factor, and α is the frequency shift factor. The three coefficients are derived from the following equations:

$$d_x(x) = d_0\left(\frac{x}{L}\right)^{P_d}, \tag{11}$$

$$\beta_x(x) = 1 + (\beta_0 - 1)\left(\frac{x}{L}\right)^{P_\beta}, \tag{12}$$

$$\alpha_x(x) = \alpha_0\left[1 - \left(\frac{x}{L}\right)^{P_\alpha}\right]. \tag{13}$$

Here, L signifies the PML thickness, while d_0, β_0, α_0, P_d, P_β and P_α are empirical coefficients derivable from established formulas. Likewise, the complex stretching functions s_y and s_z in the y and z directions can be similarly determined, along with the transformation matrices Σ and Λ,

$$\Sigma(u,v,w) = \begin{bmatrix} s_u & 0 & 0 \\ 0 & s_v & 0 \\ 0 & 0 & s_w \end{bmatrix}, \tag{14}$$

$$\Lambda(u,v,w) = \begin{bmatrix} s_v s_w & 0 & 0 \\ 0 & s_u s_w & 0 \\ 0 & 0 & s_u s_v \end{bmatrix}. \tag{15}$$

Using (u,v,w) to denote the new coordinates after the transformation, we obtain the following results:

$$E(x,y,z) \to \Sigma E_{\mathrm{PML}}(u,v,w), \tag{16}$$

$$H(x,y,z) \to \Sigma H_{\mathrm{PML}}(u,v,w). \tag{17}$$

The original Maxwell wave equations read

$$\nabla \times E(x,y,z) = -\mathrm{i}\omega_0 \mu H(x,y,z), \tag{18}$$

$$\nabla \times H(x,y,z) = \mathrm{i}\omega_0 \varepsilon E(x,y,z) + J(x,y,z). \tag{19}$$

The wave equations after the coordinate transformation are as follows:

$$\nabla \times (\Sigma E_{\mathrm{PML}}(u,v,w)) = -\mathrm{i}\omega_0 \Lambda \mu \Sigma^{-1}(\Sigma H_{\mathrm{PML}}(u,v,w)), \tag{20}$$

$$\nabla \times (\Sigma H_{\mathrm{PML}}(u,v,w)) = \mathrm{i}\omega_0 \Lambda \varepsilon \Sigma^{-1}(\Sigma E_{\mathrm{PML}}(u,v,w)) + \Lambda J(u,v,w). \tag{21}$$

Since the process of coordinate transformation does not alter physical laws, the physical quantities of the wave equation should remain equivalent before and after the transformation

$$\mu_{\mathrm{PML}} = \Lambda \mu \Sigma^{-1}, \tag{22}$$

$$\varepsilon_{\mathrm{PML}} = \Lambda \varepsilon \Sigma^{-1}. \tag{23}$$

This results in the formulation of the dielectric and permeability tensors within the PML boundary layer.[24,30]

2.3. Finite element solution of the electric field wave equation

Using the weighted residual method to solve the electric field wave equation, we assume an approximate solution ($\tilde{\boldsymbol{E}}$) and substitute it into Eq. (7). This approach enables us to identify the discrepancy between the predicted and actual values, which is defined as the residual, $\boldsymbol{R}$, as follows:

$$\boldsymbol{R} = \nabla \times \nabla \times \tilde{\boldsymbol{E}} - \omega_0^2 \mu \varepsilon \tilde{\boldsymbol{E}} - \mathrm{i}\omega_0 \mu \boldsymbol{J}. \tag{24}$$

Let the weighted integral value be equal to 0, resulting in

$$\boldsymbol{I} = \int_\Omega w \boldsymbol{R} \mathrm{d}\Omega = 0. \tag{25}$$

Considering the Galerkin method, we use basis functions as the weight functions. Within the grid elements, the basis functions are the following shape functions N:

$$\int_\Omega N \boldsymbol{R} \mathrm{d}\Omega = 0. \tag{26}$$

By performing the coordinate transformation $(x,y) \to (s,t)$, we can transform a general triangular element Ω into a reference triangular element U. This transformation results in the corresponding shape functions being expressed in the reference element, along with their respective vector form:

$$N_1 = 1 - s - t, \quad N_2 = s, \quad N_3 = t, \tag{27}$$

$$\boldsymbol{N} = [1 - s - t, s, t]. \tag{28}$$

Find the partial derivative of the shape function N with respect to s and t,

$$\frac{\partial N}{\partial s} = \begin{bmatrix} -1 \\ 1 \\ 0 \end{bmatrix}^{\mathrm{T}}, \quad \frac{\partial N}{\partial t} = \begin{bmatrix} -1 \\ 0 \\ 1 \end{bmatrix}^{\mathrm{T}}. \tag{29}$$

The expansion of Eq. (26) yields the following integral equation regarding I_x:

$$I_x = \iint N\left[-\left(\partial_y^2 + \omega_0^2 \mu \varepsilon_{xx}\right) E_x + \partial_x \partial_y E_y + \mathrm{i}\omega_0 \mu J_x\right] \mathrm{d}\Omega - \int N \frac{\partial E_x}{\partial n} \mathrm{d}\Gamma = 0. \tag{30}$$

Here, Γ denotes the boundary of the element Ω. The boundary integral term is equal to zero for linear basis functions N. Consequently, the integral equation is transformed into a weak form through integration by parts, requiring only the existence of the first derivative of the basis functions.

$$\iint \left[\partial_y N \partial_y E_x - \omega_0^2 \mu \varepsilon_{xx} N E_x - \partial_x H \partial_y E_y\right] \mathrm{d}\Omega - \iint \left(\frac{\mathrm{d}(N \partial_y E_x)}{\mathrm{d}y} - \frac{\mathrm{d}(N \partial_y E_y)}{\mathrm{d}x}\right) \mathrm{d}x\mathrm{d}y = -\mathrm{i}\omega_0 \mu \int_\Omega N J_x \mathrm{d}\Omega. \tag{31}$$

Applying Green's theorem to the above expression yields:

$$\iint \left[\partial_y N \partial_y E_x - \omega_0^2 \mu \varepsilon_{xx} N E_x - \partial_x N \partial_y E_y\right] \mathrm{d}\Omega$$

$$+\int (N\partial_y E_x \mathrm{d}x + N\partial_y E_y \mathrm{d}y)$$
$$= -\mathrm{i}\omega_0\mu \int NJ_x \mathrm{d}\Omega. \tag{32}$$

At the boundary, where the shape function $N = 0$, the boundary integral term becomes 0. Consequently, this leads to the following integral equation:

$$\iint \left[\partial_y N\partial_y E_x - \omega_0^2\mu\varepsilon_{xx}NE_x - \partial_x N\partial_y E_y\right] \mathrm{d}\Omega$$
$$= -\mathrm{i}\omega_0\mu \int_\Omega NJ_x \mathrm{d}\Omega. \tag{33}$$

Then, using numerical integration, calculate the integral values of the elements in the 4×4 matrix from the expression above. Substitute the results into the weighted residual integral equation to obtain the coefficients of the element matrix and the element vector.

For the coefficient matrix of the quadrilateral element, it is sufficient to replace the shape functions with the quadrilateral ones below:

$$N_1 = (1-s)(1-t)/4,\ \ N_2 = (1+s)(1-t)/4,$$
$$N_3 = (1+s)(1+t)/4,\ \ N_4 = (1-s)(1+t)/4, \tag{34}$$
$$\boldsymbol{N} = [(1-s)(1-t), (1+s)(1-t), (1+s)(1+t),$$
$$(1-s)(1+t)]/4. \tag{35}$$

In a similar manner, the matrix coefficients and vectors for the quadrilateral element can be derived. Subsequently, by assembling all the element matrices and vectors based on the enumeration of the mesh elements, we construct the system matrix and vector. This process results in a linear system for solving the electric field wave equation using the finite element method for the specific problem. The electric field distribution is then determined by utilizing MATLAB built-in linear equation solver library.

3. Simulation results and discussion

Figure 3 shows the calculated electric field distributions (E_y and E_z) under three toroidal phases of the antenna. The periodic spatial distribution of E_y and E_z fields and their phase difference indicate that the electromagnetic waves (fast waves) generated by the RF antenna propagate into the plasma. When changing the phase of the RF antenna, significant changes occur in the spatial distribution of the radiated electric field. When the phase differences between adjacent antennas in the toroidal direction are $\pi, \pi/2$ and 0, the FW radiated electric fields (E_y and E_z) exhibit anti-symmetric (they have the same absolute values, but their directions are opposite on the right and left sides), asymmetric, and symmetric distributions in the toroidal direction, respectively. However, the radial field E_y is stronger than the poloidal field E_z at 3 phase configurations.

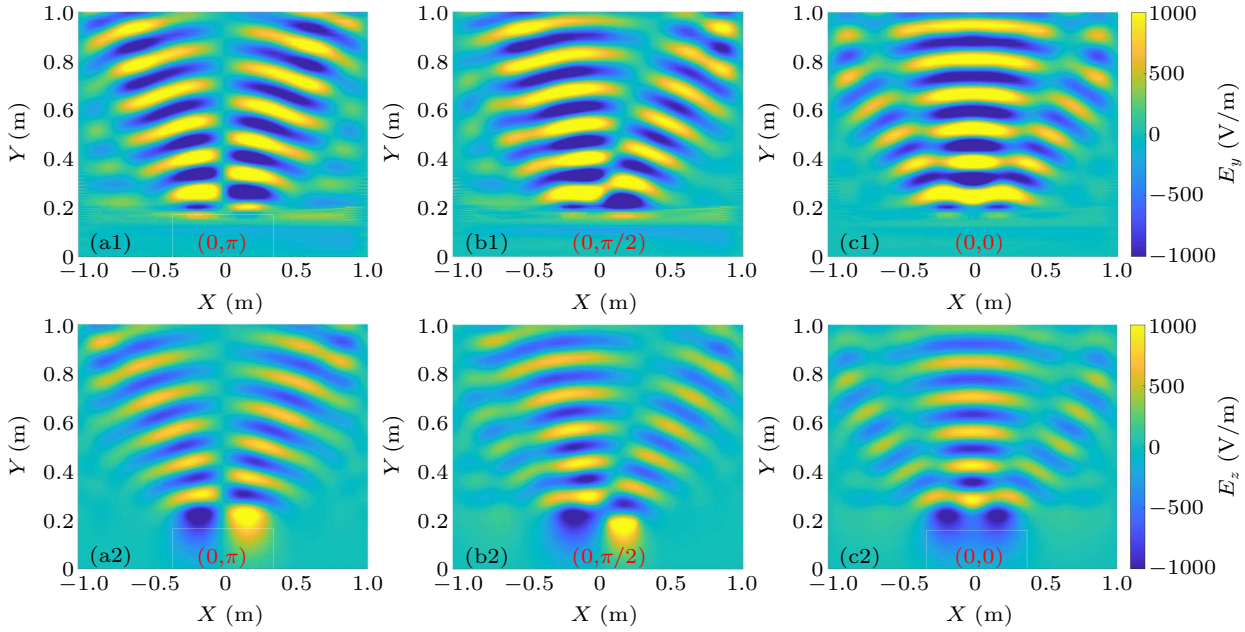


Fig. 3. The real parts of the E_y and E_z fields excited under 3 phases of the RF antennas. The first row is radial electric field E_y; the second row poloidal electric field E_z.

Under 3 antenna phases, the direction of energy propagation of the electromagnetic waves radiated by the antenna varies, corresponding to different radiation patterns and $k_\parallel$. By performing a Fourier transform on the simulated electromagnetic fields, the parallel power spectrum is calculated and plotted in Fig. 4.

When the toroidal phase difference of the RF antenna is π $(0,\pi)$, the excited RF power reaches a peak value at $k_\parallel \sim 9\ \mathrm{m}^{-1}$. Furthermore, when the toroidal phase difference is $\pi/2$ $(0,\pi/2)$, the main peak value is maximized, and the full

width at half maximum is minimized. When the toroidal phase difference is either $\pi/2$ or π, the peaks are widely spaced and distinct from each other. In contrast, when the phase difference is 0 (0, 0), two main peak regions are closely situated, which may lead to partial overlap in their spectra. The power spectra for phase differences of 0 and π exhibit a symmetrical distribution, whereas the case of phase difference $\pi/2$ displays an asymmetrical distribution. This asymmetry corresponds to the electric field distributions illustrated in Fig. 3. The calculated electric field distributions and power spectra exhibit qualitative consistency with the results reported in Refs. [10,24,26] due to similar antenna configurations. This alignment partly supports the reliability of our model.

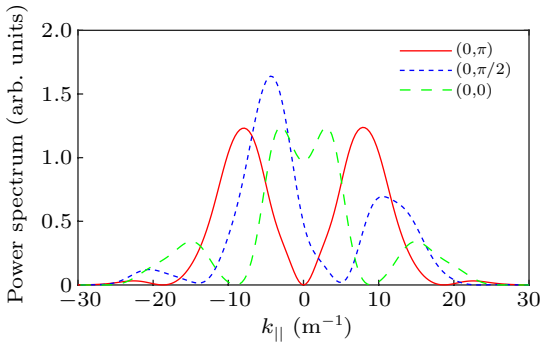


Fig. 4. The $k_{||}$ power spectrum emitted under 3 antenna phase configurations.

4. Conclusion

In this study, we developed a two-dimensional ICRF antenna simulation code (ICRAEMS) using the MATLAB platform. This code is designed for cold plasma environments in a tokamak, utilizing a magnetized cold plasma approximation dielectric tensor to account for plasma anisotropy. A PML boundary condition is implemented to facilitate a single-pass model, and the electric field wave equation is solved by using the finite element method. Triangular meshing is employed in the antenna and electromagnetic field propagation regions, with local mesh refinement near the antenna to accommodate the geometric structures of various complex antennas while ensuring the accuracy of the electric field solutions. In the areas within the PML layer, a regular quadrilateral mesh is used to optimize the performance of the PML, ensuring complete absorption of electromagnetic waves.

The input parameters for the model geometry are derived from open-source meshing software, enabling the code to efficiently simulate different antenna geometrical structures. Furthermore, the propagation of radio frequency waves under varying antenna phases and plasma parameter conditions is investigated, allowing for an analysis of how different operational parameters affect antenna coupling characteristics. The results indicate significant differences in electric field and power spectrum distributions across three antenna phase scenarios. The calculated results achieve qualitative agreement with existing literature, thereby validating the reliability of the model.

Program availability

The source code is openly available in the Science Data Bank at https://doi.org/10.57760/sciencedb.j00113.00175

Acknowledgments

Project supported by the National MCF Energy R&D Program (Grant No. 2022YFE03190100), the National Natural Science Foundation of China (Grant Nos. 12422513, 12105035, and U21A20438), and the Xiaomi Young Talents Program.

References

[1] Zhang X J, Qin C M, Liu L N, Zhao Y P, Mao Y Z, Yang H, Lv B, Chang J F, Huang J, Wang L, Yuan S, Deng X, Chen G, Cheng Y, Ju S Q, Zhang K, Yuan J A, Li M H, Ding B J, Gong X Z, Wan B N, Song Y T, Li J G, Ai L, Ping L L and EAST team 2020 *AIP Conf. Proc.* **2254** 030004

[2] Wang J H, Chen G, Zhao Y P, Mao Y Z, Yuan S, Zhang X J, Yang H, Qin C M, Cheng Y, Yang Y Q, Urbanczyk G, Liu L N and Cheng J 2018 *Plasma Sci. Technol.* **20** 045603

[3] Liu L N, Zhang X J, Zhu Y B, Qin C M Qin, Zhao Y P, Yuan S, Mao Y Z, Li M H, Chen Y, Cheng J, Ping L L, Li H and Ai L 2019 *Rev. Sci. Instrum.* **90** 063504

[4] Porkolab M, Becouletz A, Bonoliy P T, Gormezanox C, Kochk R, Majeski R J, Messiaenk A, Noterdaeme J M, Petty C, Pinsker R, Start D and Wilson R 1998 *Plasma Phys. Control. Fusion* **40** A35

[5] Petty C C, Baity F W, deGrassie J S, Mau T K, Pinsker R I, Porkolab M and Prater R 2001 *Plasma Phys. Control. Fusion* **43** 1747

[6] Yin L, Yang C, Gong X Y, Lu X Q, Du D and Chen Y 2017 *Phys. Plasmas* **24** 102502

[7] Hosea J, Bell R E, LeBlanc B P, Phillips C K, Taylor G, Valeo E, Wilson J R, Jaeger E F, Ryan P M, Wilgen J, Yuh H, Levinton F, Sabbagh S, Tritz K, Parker J, Bonoli P T, Harvey R and NSTX Team 2008 *Phys. Plasmas* **15** 056104

[8] Pinsker R I, Porkolab M, Heidbrink W W, Luo Y, Petty C C, Prater R, Choi M, Schaffner D A, Baity F W, Fredd E, Hosea J C, Harvey R W, Smirnov A P, Murakami M and Van Zeeland M A 2006 *Nucl. Fusion* **46** S416

[9] Ono M 1995 *Phys. Plasmas* **2** 4075

[10] Qin C M, Zhang X J, Zhao Y P, Wan B N, Braun F, Wang L, Yang Q X, Yuan S. and Cheng Y 2015 *Plasma Sci. Technol.* **17** 167

[11] Pécoul S, Heurauxa S, Kochb R and Leclert G 2002 *Computer Physics Communications* **146** 166

[12] Yang H, Zhang X J, Qin C M, Zhao Y P, Yuan S, Mao Y Z, Yang X, Li M H, Urbanczyk G, Wang M, Wang X J, Xu H D, Ding B J, Li Y C, Xu G S, Hu L Q, Ai L and Guo Y Y 2021 *Nucl. Fusion* **61** 035001

[13] Clairet F, Colas L, Heuraux S and Lombard G 1993 *Plasma Phys. Control. Fusion* **35** 1481

[14] Jacquet P, Bobkov V, Mayoral M L, Monakhov I, Noterdaeme J M, Scarabosio A, Stepanov I, Vrancken M, Wolfrum E and the ASDEX Upgrade team 2012 *Nucl. Fusion* **52** 042002

[15] Carter M D, Wang C Y, Hogan J T, Harris J H, Hoffman D J, Rasmussen D A, Ryan P M, Stallings D S, Batchelor D B, Beaumont B, Hutter T and Saoutic B 1996 *AIP Conf. Proc.* **355** 364

[16] Milanesio D, Helou W, Polli V, DurodiéF, Lamalle P, Louche F and Zhang W 2023 *AIP Conf. Proc.* **2984** 060008

[17] Milanesio D and Maggiora R 2010 *Nucl. Fusion* **50** 025007

[18] Milanesio, Helou W, Polli V, Durodié F, Lamalle P, Maquet V, Messiaen A, Tierens W and Zhang W 2023 *Nucl. Fusion* **63** 046010

[19] Lancellottia V, Milanesio D, Maggiora R, Vecchi G and Kyrytsya V 2006 *Nucl. Fusion* **46** S476

[20] Usoltceva M, Tierens W, Kostic A, Noterdaeme J M, Ochoukov R and Zhang W 2016 *AIP Conf. Proc.* **2254** 050003

[21] Usoltceva M, Ochoukov R, Tierens W, Kostic A, Crombé K, Heuraux S and Noterdaeme J M 2019 *Plasma Phys. Control. Fusion* **61** 115011

[22] Tierens W, Milanesio D, Urbanczyk G, Helou W, Bobkov V, Noterdaeme J M, Colas L, Maggiora R, the ASDEX Upgrade team and the EUROfusion MST1 team 2019 *Nucl. Fusion* **59** 046001

[23] Tierens W, Suárez López G, Otin R, Urbanczyk G, Colas L, Bilato R, Zhang W, Bobkov V and Noterdaeme J M 2020 *AIP Conf. Proc.* **2254** 070005

[24] Jacquot J, Colas L, Clairet F, Goniche M, Heuraux S, Hillairet J, Lombard G and D Milanesio 2013 *Plasma Phys. Control. Fusion* **55** 115004

[25] Lu L, Crombé K, Van Eester D, Colas L, Jacquot J and Heuraux S 2016 *Plasma Phys. Control. Fusion* **58** 055001

[26] Yang H, Wu C F, Dong S, Zhao Y P, Zhang X J and Shang L 2016 *Nucl. Sci. Tech.* **27** 46

[27] Li J H, Yang Q X, Song Y T, Yu C, Chen S L, Xu H and Du D 2021 *Journal of Nuclear Science and Technology* **58** 837

[28] Du D 2015 *Theoretical Analysis of The Interaction Between ICRH Antenna System and Plasma* (Ph.D. Dissertation) (Hengyang: University of South China) (in Chinese)

[29] Berenger J P 1994 *Journal of Computational Physics* **114** 185

[30] Colas L, Jacquot J, Hillairet J, Helou W, Tierens W, Heuraux S, Faudot E, Lu L and Urbanczyk G 2019 *Journal of Computational Physics* **389** 94